


Cite this: *Nanoscale Adv.*, 2025, 7, 5323

# Novel self-assembled valine-derived carbon-supported Ag@ZnO optical materials for enhanced photodegradation and anti-bacterial activity

P. R. Nithiasri, J. Aarthi and B. Karthikeyan \*

Herein, the synthesis of self-assembled amino acid valine-derived carbon-supported silver–zinc oxide (C–Ag@ZnO), Ag@ZnO and ZnO nanoparticles through a sol–gel method is reported. X-ray diffraction (XRD), Fourier transform infrared (FT-IR) spectroscopy, X-ray photoelectron spectroscopy (XPS), high-resolution transmission electron microscopy (HRTEM), electron paramagnetic resonance (EPR) and UV-vis diffuse reflectance spectroscopy (UV-DRS) were used to investigate the characteristics of C–Ag@ZnO nanocomposites. The rapid charge carrier recombination and dependence on ultraviolet (UV) radiation limit the effectiveness of zinc oxide (ZnO) nanoparticles for environmental cleaning. In order to overcome these difficulties, carbon doping has been suggested as a way to improve charge separation and visible light absorption, and metal nanoparticle doping, such as silver nanoparticle doping, can enhance photocatalytic activity and antibacterial activity. In this work, the photodegradation of brilliant blue (BB) was used to measure the C–Ag@ZnO nanocomposite photocatalytic activity. Improved photocatalytic activity was obtained for C–Ag@ZnO nanoparticles compared to other pristine nanocomposite Ag@ZnO and pristine ZnO. Further it has been demonstrated that an optimum amount of self-assembled carbon along with silver doping is necessary to achieve a significant antibacterial and photocatalytic activity. The role of self-assembly is reported herein for the first time.

Received 1st May 2025  
Accepted 9th July 2025

DOI: 10.1039/d5na00427f

rsc.li/nanoscale-advances

## 1. Introduction

Multiple research investigations have been conducted on the photocatalytic removal of organic pollutants released from the textile, leather, and hair coloring industries because of its significant potential to form non-toxic end products, ease of preparation, and effectiveness. There are four steps involved in the photoreaction when the catalyst is present.<sup>1</sup> Particularly, organic textile dyes are toxic, indestructible, bio-recalcitrant, fade-resistant, and significantly harmful to human health.<sup>2–4</sup> However, the implementation of these physical and chemical techniques is constrained by a number of issues, including selectivity, low removal efficiency, energy intensity, and partial dye removal.<sup>5,6</sup> The photodegradation of organic contaminants in water using single and ternary metal-oxide catalysts is a significant purification technique.<sup>7–9</sup> Gas sensors, fuel cells, batteries, higher-temperature superconducting materials and microelectronic circuits are merely a few of the inventions that use nano-metal oxides. They also serve as antimicrobials, absorbents, and catalysts owing to their large surface area and small size, which improve their conductivity and electrical and catalytic properties.<sup>10–13</sup> Transition metals are frequently doped to create

nano-composites with enhanced photocatalytic activity by generating surface oxygen vacancies, enhancing UV-visible absorption, and inhibiting charge center recombination.<sup>14</sup> To remove dyes from wastewater, a variety of methods such as coagulation, chemical extraction, adsorption, hyper filtration (reverse osmosis), filtration, precipitation, and photodegradation have been used.<sup>15–19</sup> Adsorption of dyes is appealing since it is inexpensive, highly effective, simple to use, and requires a small amount of sludge to be disposed away.<sup>20</sup> Currently, complex organic contaminants and colors are removed under UV light using advance oxidation processes (AOPs) such photocatalysis.<sup>21–24</sup> By generating surface oxygen vacancies, inhibiting charge center recombination, and expanding UV-visible absorption, doping nano composites with transition metals to increase their photocatalytic activity is an established method.<sup>25</sup> Silver has been shown to improve semiconductor nanoparticles' photocatalytic activity.<sup>26</sup> Industrial effluent degradation is found to benefit from ZnO's stability, wide bandwidth, and high photosensitivity.<sup>27,28</sup> ZnO functions as a catalyst in the treatment of wastewater and exhibits antimicrobial qualities when added to coatings, textiles, *etc.*<sup>29</sup> ZnO normally features large holes and light electrons, which is a fundamental property of an n-type semiconductor, based on the effective mass calculation. However, loading with N, C, and S can typically make large holes and lighter electrons, which slows down the rate at which photogenerated hole–electron pairs recombine.<sup>30</sup> The use of organic solvents or organic substances has created

Department of Chemistry, Annamalai University, Annamalai Nagar, Tamil Nadu, 608002, India. E-mail: India.bkarthi\_au@yahoo.com; aarthijeevanantham@gmail.com

a difficulty with carbon doping sources, which has increased the costs of synthetic materials even though the sectors have been driven by the remarkable advantages of C-doped ZnO. The vitamin C compound, 2-methylimidazole, aniline and ethylene glycol are all listed.<sup>31</sup> Wand *et al.* synthesized ZnO powder of various sizes by both chemical and physical techniques.<sup>32</sup> In a work by Hong *et al.*, co-precipitation was used to fabricate an Fe<sub>3</sub>O<sub>4</sub>/ZnO core shell nanocomposite, and in 6 hours, 83% of MO was photodegraded.<sup>33</sup> In Fu *et al.*'s study, Cu-doped ZnO nanoparticles were synthesized, which showed 88% MO decomposition in 4 hours.<sup>34</sup> Sabry *et al.* synthesized Ag-ZnO by co-precipitation, and the dye degradation was 93%.<sup>35</sup> Kwon *et al.* reported the synthesis of Ag-ZnO (0.05–0.5%) by a hydrothermal method, and the dye degradation was 92.9%.<sup>36</sup> Ebrahimi *et al.* synthesized Ag-ZnO (2.5%) by a thermosolvent method, for which the dye degradation was 74%.<sup>37</sup> Gnanaprakasam *et al.* synthesized Ag-ZnO (1–3%) by co-precipitation, showing 88% dye degradation.<sup>38</sup> Pradeevraj *et al.* reported Mg-ZnO synthesized by co-precipitation, which exhibited 78% dye degradation.<sup>39</sup> According to this work, when Brilliant Blue dyes are exposed to visible light, the produced C-Ag@ZnO nanocomposites exhibit enhanced photocatalytic ability compared to Ag@ZnO and ZnO. The synergistic interaction between C-Ag@ZnO, Ag@ZnO and ZnO, which leads to a delayed electron-hole recombination rate and a prolonged light absorption ability, may result in improved photocatalytic performance. Additionally, a thorough photocatalytic mechanism is suggested to account for the enhanced photocatalytic activity. The role of self-assembled carbon derived from amino acid is reported for the first time.

## 2. Experimental section

### 2.1 Synthesis of C-Ag@ZnO, Ag@ZnO, pristine ZnO nanoparticles and self-assembled L-valine carbon

L-Valine (1 M) was dispersed in 100 mL deionized water. It was heated in a hot plate with a magnetic stirrer in a silicone oil bath at 60 °C for 30 min. Then, it was allowed to cool to room temperature. The self-assembled L-valine solution was kept in the hot plate to evaporate the solution to obtain a self-assembled L-valine powder form. In a muffle furnace, the acquired material was further charred at 300 °C for 2 h. Using a mortar and pestle, the resulting brown powder was thoroughly

ground into a uniform form. The acquired compound is self-assembled carbon. Similarly, carbon, zinc nitrate hexahydrate, silver nitrate, citric acid, and ammonium solution were mixed and subjected to a sol-gel synthesis process (Scheme 1). The ratio of carbon, zinc nitrate hexahydrate, and silver nitrate were 0.1, 0.3 and 0.1 (M), and C-Ag@ZnO nanocomposites are produced by carbonizing them in a tube furnace at 500 °C. The same sol-gel method was adopted for pristine ZnO and Ag@ZnO nanoparticle synthesis. By employing a variety of characterisation techniques, all materials were thoroughly examined.

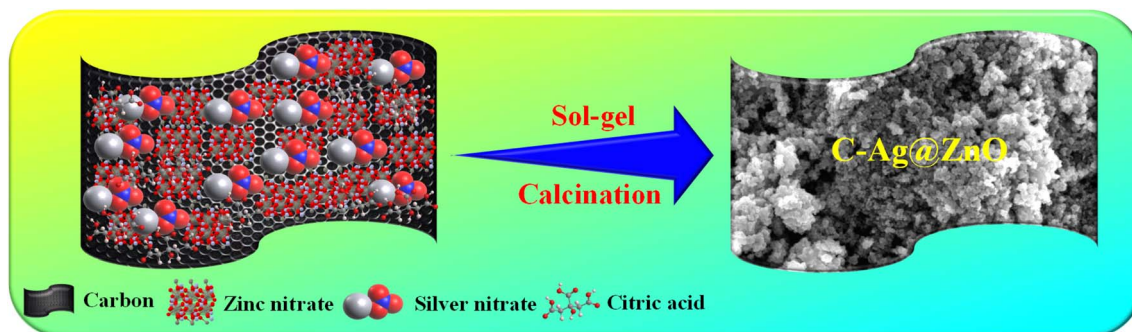
### 2.2 Physical characterization

The prepared sample was characterized by X-ray diffraction (XRD) using a BRUKER ECO D8 ADVANCE diffractometer, Fourier Transform Infrared (FT-IR) spectroscopy using a Shimadzu IR Tracer 100, FE-SEM using a CARL ZEISS-SIGMA 300 equipped with an EDX spectrometer at 0.02 kV to 30 kV, high-resolution transmission electron microscopy (HR-TEM) and selected area electron diffraction (SAED) using a JEM-2100 Plus, XPS using a thermo scientific instrument (K-Alpha-KAN9954133), Raman spectroscopy using a Micro Raman Spectrometer-STR at 500 nm, UV-DRS using a SHIMADZU/UV 2600, photoluminescence using a Perkin-LS 45, electron paramagnetic resonance (EPR) using a Bruker EMX Plus, and BET (Brunauer-Emmett-Teller) analysis using Quantachrome Instruments version 5.25.

### 2.3 Photocatalytic degradation studies

For photodegradation, Brilliant Blue dye was subjected to UV chamber irradiation and used to thoroughly examine the material photocatalytic activity. Reaction tubes were filled with 100 mL of  $1 \times 10^{-4}$  concentration of an aqueous suspension of BB dye and 100 mg of the photocatalyst. UV light was applied to the solution. The solution mixture was let out to UV-vis spectrophotometer with wavelength range of 200 to 800 nm to measure the absorbance changes. Then, 4 mL of the reaction mixture was taken every 15 minutes. The wavelength range of brilliant blue dye was 556 nm, and the degradation efficiency was calculated using eqn (1):

$$\text{Degradation rate (\%)} = (C_0 - C_t/C_0) \times 100 \quad (1)$$



Scheme 1 Schematic of the C-Ag@ZnO synthesis.



At a specific reaction time ( $t$ ), the initial and final concentrations of the dye are denoted by  $C_0$  and  $C_t$ , respectively.<sup>40</sup>

## 2.4 Antibacterial assay

The prepared catalysts (ZnO, Ag@ZnO, and C-Ag@ZnO) were tested using an agar well diffusion method to determine their antibacterial activity against *Salmonella typhi*, *Bacillus subtilis*, *Enterococcus faecalis*, and *Klebsiella pneumoniae*. After being incubated for 24 hours at 38 °C in a Mueller–Hinton broth that had already been sterilized, the pathogens produced turbidity, which was a sign of bacterial growth. Using a 6 mm cork borer, wells were made and clinical bacterial strains were separately plated onto Mueller–Hinton agar for further incubation. As positive and negative controls, respectively, azithromycin and DMSO were employed. The zone of inhibition (mm) for the antibacterial activity of the prepared compound was displayed.<sup>41,42</sup> The efficiency of the nanoparticles against the bacterial strains was assessed by measuring the zone of inhibition using the antibiotic zone scale after the incubation period. Three distinct concentrations (75  $\mu$ L, 150  $\mu$ L, and 300  $\mu$ L) were used to record the data appropriately.

## 3. Results and discussion

### 3.1 Crystallographic and vibrational properties

From the sol–gel method route and calcination at 400 °C, the obtained composition of C-Ag@ZnO is analysed. The crystal

structure and morphology after C-Ag@ZnO doping were characterized by XRD, FTIR spectroscopy, Raman spectroscopy, FE-SEM and HR-TEM. The Bragg angles and diffraction intensity of C-Ag@ZnO consistent with ZnO (JCPDS No. 36-1451) peaks were located at diffraction peaks at  $2\theta$  degrees of 31°, 34°, 36°, 47°, 56°, 63°, 66°, 68°, 69°, 72°, and 77° assigned to the (100), (002), (101), (102), (110), (103), (200), (112), (201), (004) and (202) plane values are denoted.<sup>43</sup> Ag (JCPDS No. 04-0783) peaks located at 38.03°, 44.21° and 64.40° correspond to the (111), (200) and (202) planes, respectively.<sup>44</sup> The spectra of C-Ag@ZnO show peaks at  $2\theta^\circ = 29.0^\circ$  and  $44.8^\circ$ , which are ascribed to the (002) and (100) planes of graphitic carbon (C).<sup>45,46</sup> Here, for C-Ag@ZnO, there is a shift in carbon peak at  $2\theta$  degrees of  $27.6^\circ$  and  $44.1^\circ$ . Therefore, it is clearly confirmed that the as-prepared material is the carbon-assisted nano-metal oxide C-Ag@ZnO (Fig. 1(a)). As shown in Fig. 1(b), the FT-IR spectra were recorded between 4000 and 400  $\text{cm}^{-1}$  to validate and detect the nano-composites of ZnO, Ag@ZnO and C-Ag@ZnO. Water and surface-adsorbed hydroxyl groups (O–H) are represented by the absorption band at 3286  $\text{cm}^{-1}$ . The absorption bands at 1533 and 905  $\text{cm}^{-1}$  are associated with C=O and C=C bonds.<sup>47</sup> The occurrence of Zn–O and Ag@ZnO stretching bonds is evident from the absorbance peak observed in the spectra at around 535 and 708  $\text{cm}^{-1}$ .

The appearance of the C=O=C peak, a typical impurity detected by IR spectra, at about 2351  $\text{cm}^{-1}$  is the final observation from FT-IR spectra.<sup>48</sup>

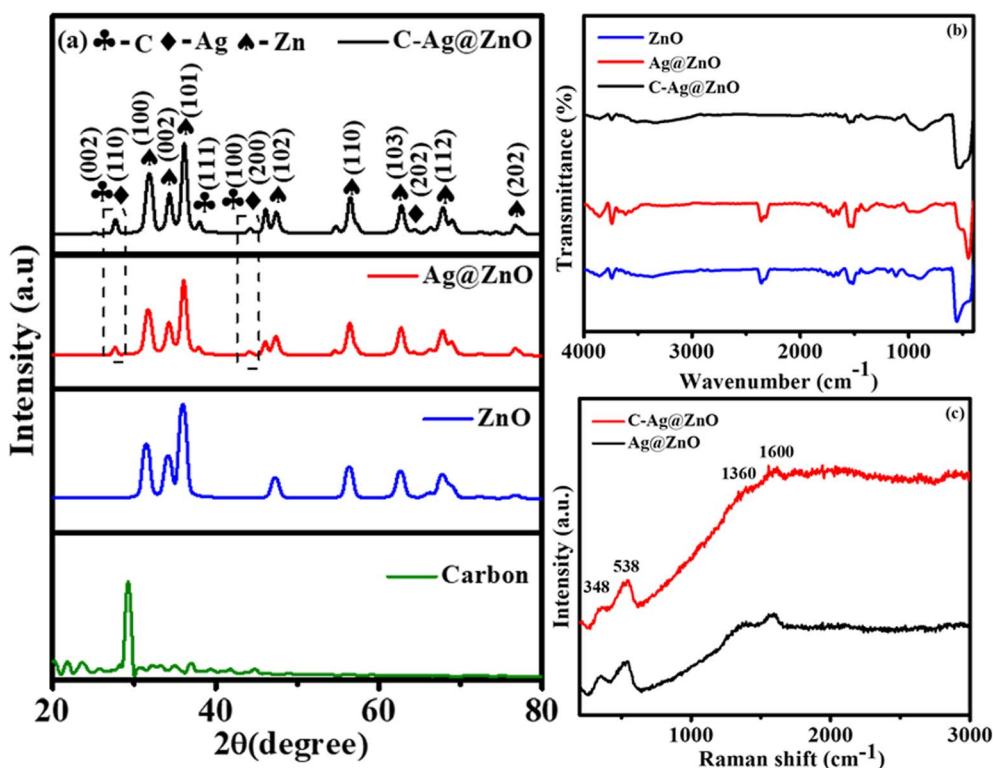


Fig. 1 (a) XRD spectra of self-assembled carbon, ZnO, Ag@ZnO and C-Ag@ZnO. (b) FTIR spectra of ZnO, Ag@ZnO and C-Ag@ZnO. (c) Raman spectra of Ag@ZnO and C-Ag@ZnO.





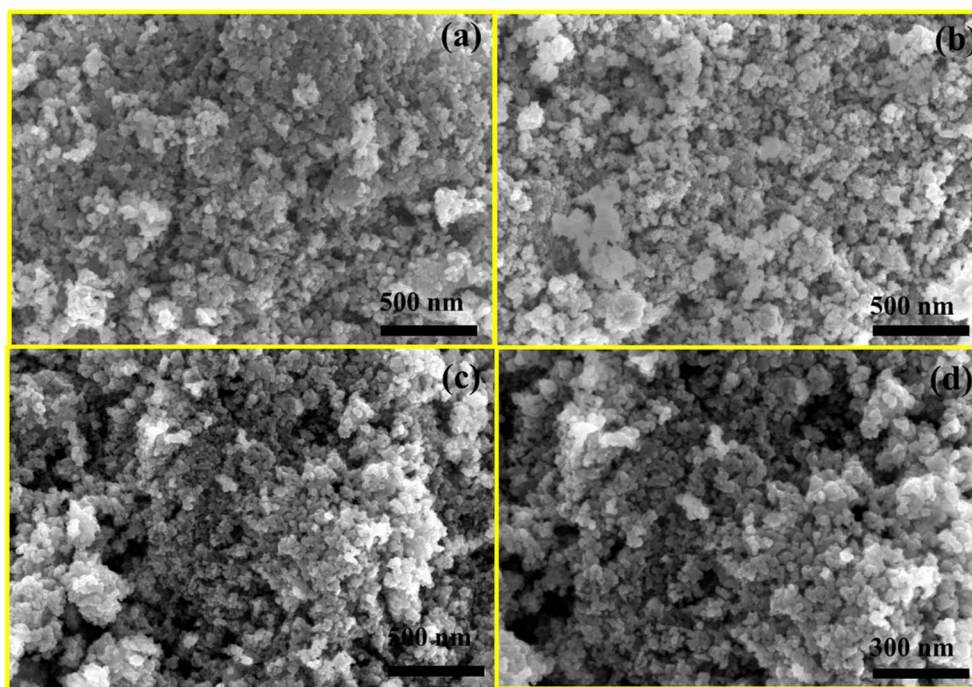


Fig. 2 FE-SEM images of ZnO (a), Ag@ZnO (b) and C-Ag@ZnO (c) and (d).

The occurrence of Raman active vibrational modes in Ag@ZnO and C-Ag@ZnO composite phases was verified by Raman spectroscopy (Fig. 1(c)). The second-order scattering from the boundary zone phonons is  $2E_2$ , and  $E_2$  and  $A_1$  (LO) are linked to the Raman-active modes of Ag@ZnO at 348 and

$538\text{ cm}^{-1}$ , respectively. The presence of Raman active vibrational modes associated with the S-A valine carbon of C-Ag@ZnO in the composite was also suggested by the appearance of G and D bands at  $1360$  and  $1600\text{ cm}^{-1}$ , which denoted the graphitic nature as well as defects in the compound.<sup>49,50</sup>

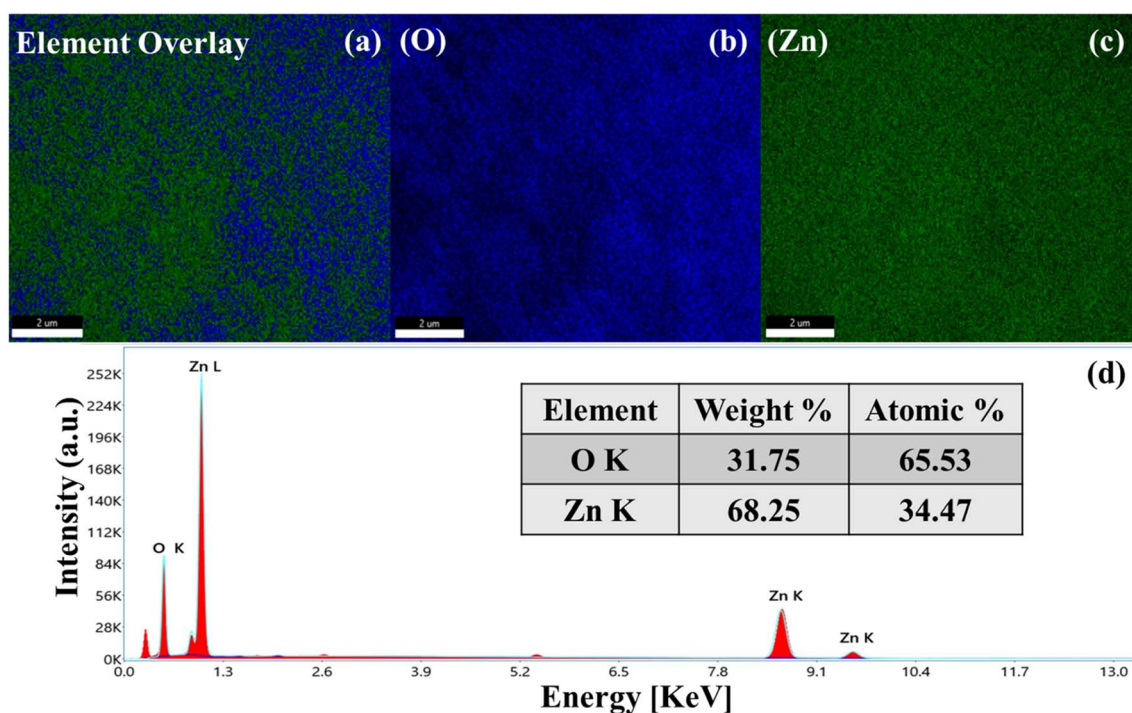


Fig. 3 (a)–(c) Elemental mapping. (d) EDX spectrum.



### 3.2 Morphology and size distribution

The nanocomposites of ZnO showed a spherical grain-like morphology (Fig. 2(a)), Ag@ZnO an agglomerated sphere-like morphology (Fig. 2(b)) and C-Ag@ZnO an irregular sphere-like morphology (Fig. 2(c) and (d)).

Furthermore, elemental mapping obviously exhibits Zn and O in ZnO (Fig. 3(a)–(c)), Zn Ag and O in Ag@ZnO (Fig. 4(a)–(d)) and C, Ag, Zn and O in C-Ag@ZnO (Fig. 5(a)–(e)), showing homogenous distribution of represented elements, and the EDX spectrum shows the elemental composition of ZnO (Zn-22.25%

and O-15.65%), Ag@ZnO (Zn-22.25%, Ag-15.65% and O-51.01%) and C-Ag@ZnO (C-22.25%, Zn-15.65%, Ag-11.09% and O-51.01%), which reveals the purity of the catalysts (Fig. 3(d), 4(e) and 5(f)).

The HR-TEM results given in Fig. 6(a) and (b) also confirm that the ZnO and Ag metal nanocomposites are well embedded into the carbon matrix. Owing to the strong reflection of the employed electron beams, the dark areas in HR-TEM examination are indicative of crystalline materials. Consequently, it can be claimed that the grey matrix in the HR-TEM analysis represents that carbon was found, whereas the black spots in

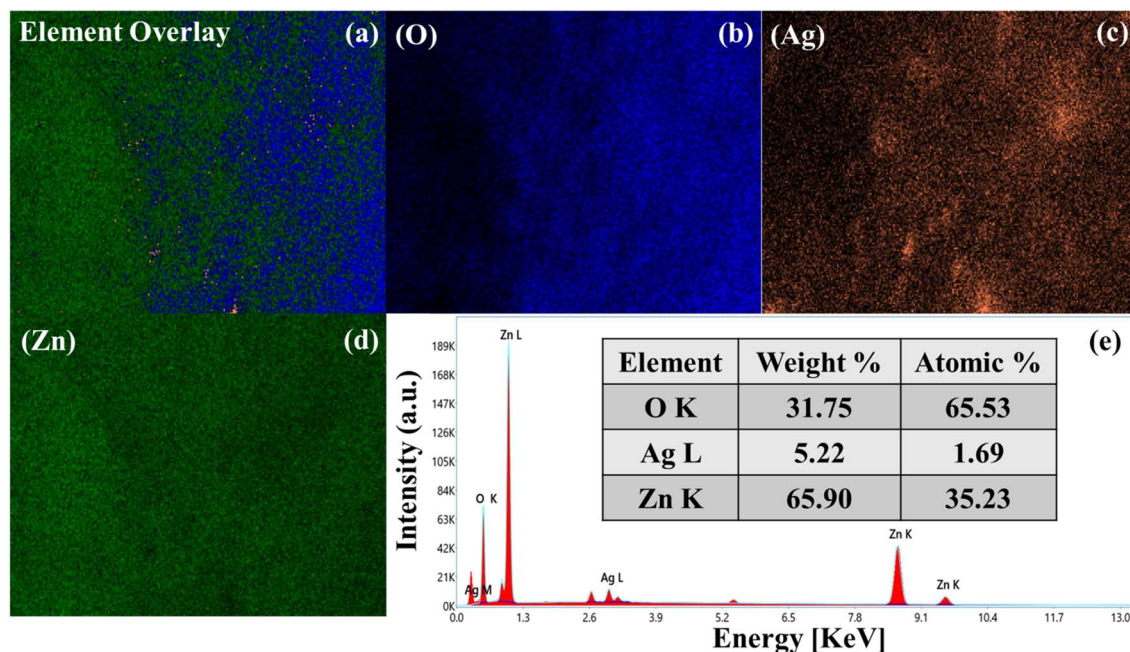


Fig. 4 (a)–(d) Elemental mapping. (e) EDX spectrum.

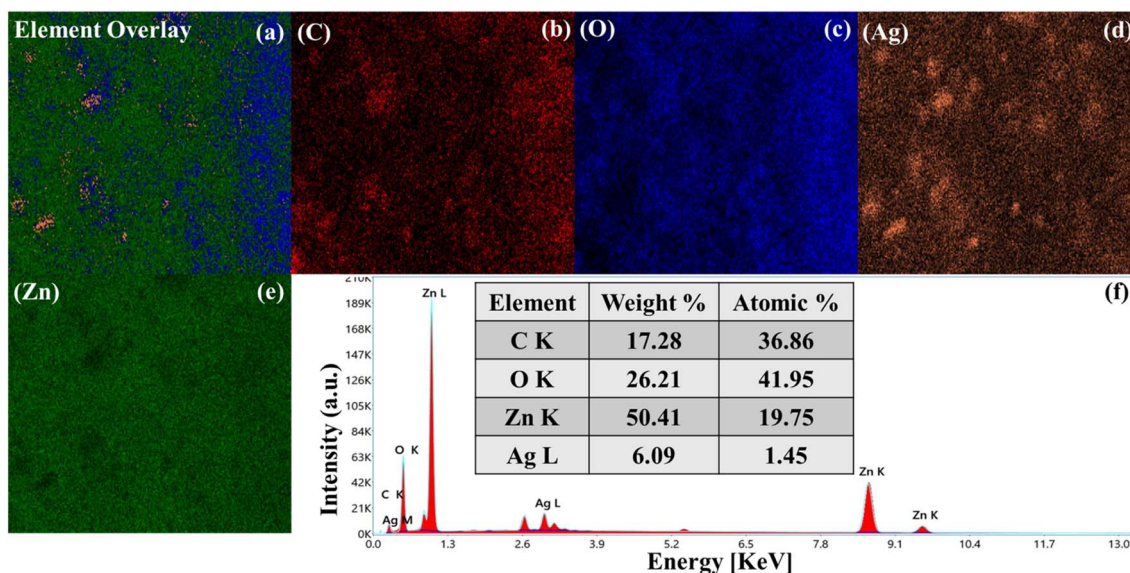


Fig. 5 (a)–(e) Elemental mapping. (f) EDX spectrum.





the synthesized nanocomposites indicate the counterpart of inorganic materials (Fig. 6(a) and (b)). The HR-TEM image shows well-resolved lattice fringes of 0.245, 0.235, and 0.334 nm assigned to the (101), (111), and (002) plane values of C-Ag@ZnO, as substantiated by XRD results (Fig. 6(c)). These facts helped to enhance the catalytic performance. The SAED image shows bright rings with discrete patches matched to the ZnO, Ag and C planes of (101), (111), and (002) (Fig. 6(d)). The average particle size was calculated for C-Ag@ZnO to be 14.3 nm.

The BET method was used to characterize the surface area and porosity of the resulting C-Ag@ZnO nanocomposite. A greater surface area was expected to indicate that a material's surface contains more atoms or molecules. In this instance,

a larger surface area and more porosity would enable higher mass transfer between the materials. The samples display type-IV isotherms with a hysteresis loop, indicating the presence of mesopores. High surface area might allow obtaining more active areas for chemical reactions during catalysis, thereby increasing the catalytic activity. Fig. 7(a) Brunauer–Emmett–Teller (BET) surface areas:  $8.194 \text{ m}^2 \text{ g}^{-1}$ . The diameters of the pore are 3.401 nm, respectively, and the pore size reduced as the cages were wrapped (Fig. 7(b)). The corresponding total pore volumes are 0.236 cc/g. The C-Ag@ZnO composite exhibits increased activity as a result of the increased surface area and porosity, which creates more active sites for the adsorption of pollutants that cause photocatalytic degradation. In addition to

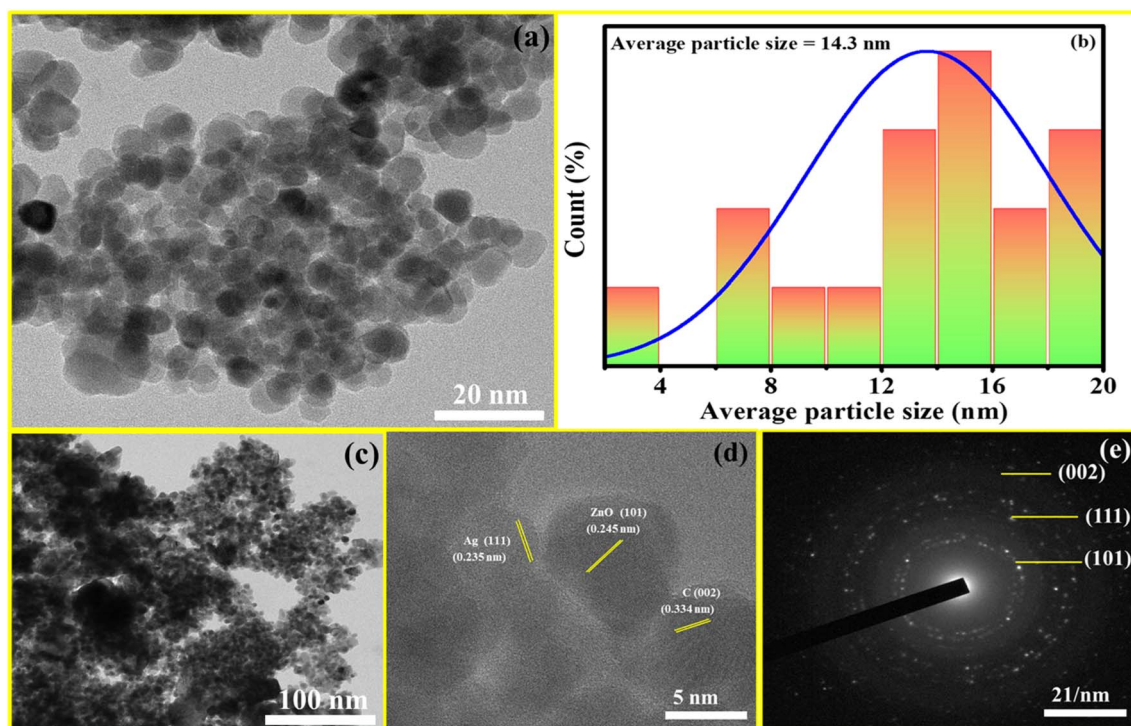


Fig. 6 HR-TEM images of C-Ag@ZnO (a) and (c), histogram (b), (d) lattice fringes and (e) SAED pattern.

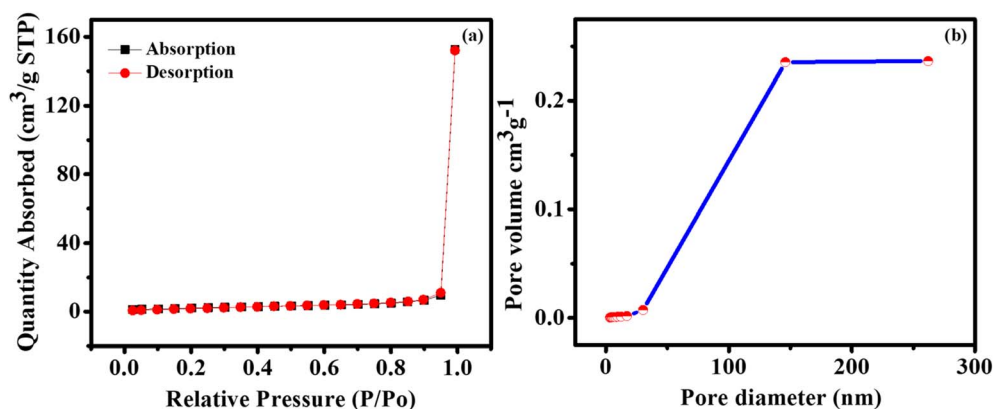


Fig. 7 (a) Nitrogen adsorption–desorption isotherms. (b) BJH patterns of C-Ag@ZnO.



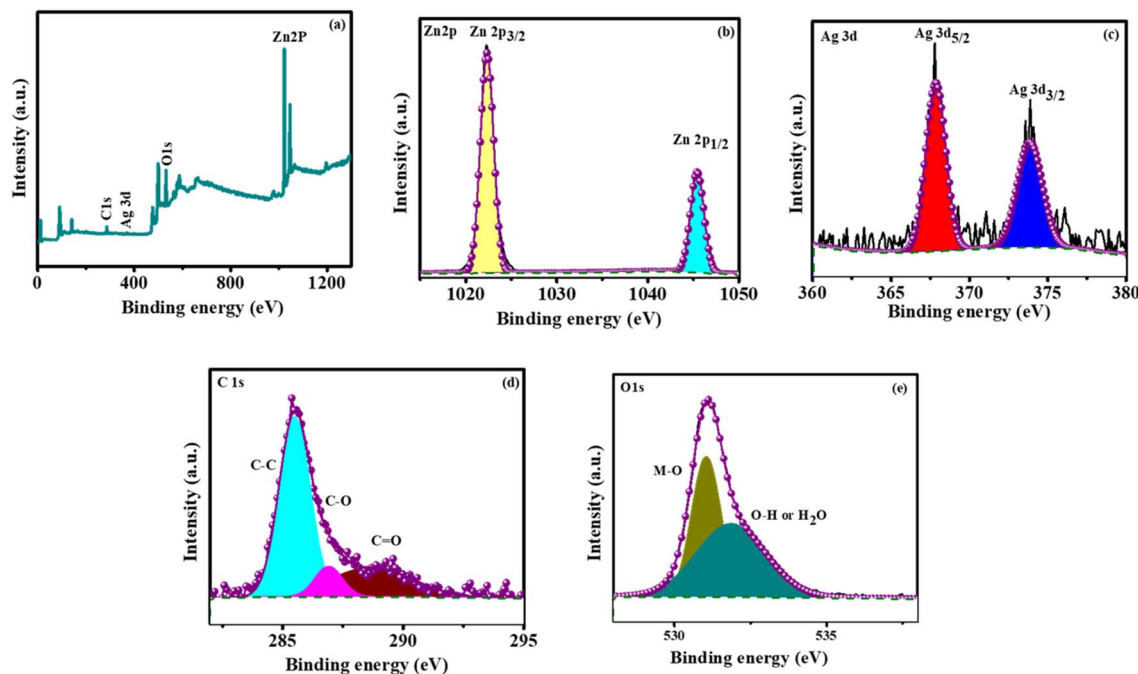


Fig. 8 HR-XPS spectra of C-Ag@ZnO: (a) survey spectrum and deconvoluted XPS spectrum of (b) Zn 2p, (c) Ag 3d, (d) C 1s and (e) O 1s orbitals.

the composite material's increased surface area and pore volume, C-Ag@ZnO provides additional sites for the diffusion of dye molecules and oxygen for consumption, enabling effective photo-catalytic degradation. The adsorption-desorption curves' type IV hysteresis loop displays an appropriately high desorption branch and decreasing adsorption, indicating the presence of mesoporous particles even at high relative pressures ( $P/P_0$ ).<sup>51</sup>

### 3.3 Chemical state characterization by XPS

The chemical state and electronic structure of C-Ag@ZnO were examined by XPS. The elements of Zn, Ag, C and O in C-Ag@ZnO were confirmed by survey scan in Fig. 8(a). The Zn 2p spectrum appears at 1022.3 eV and 1045.4 eV, which are

ascribed to Zn 2p<sub>3/2</sub> and Zn 2p<sub>1/2</sub>, respectively. These peaks demonstrate that the Zn element is present in the C-Ag@ZnO nanocomposites in a divalent cation ( $\text{Zn}^{2+}$ ) state in Fig. 8(b).<sup>52</sup> These peaks demonstrate that the Zn element is present in the C-Ag@ZnO nanocomposites in a divalent cation ( $\text{Zn}^{2+}$ ) state. Two peaks in the Ag 3d spectrum, with centers at 367.8 and 373.8 eV, are attributed to the Ag 3d<sub>5/2</sub> and Ag 3d<sub>3/2</sub> transitions, as shown in Fig. 8(c).<sup>53</sup> The deconvoluted high-resolution C 1s spectrum shows three distinct peaks at 285.1, 286.9, and 289.0 eV are ascribed to the  $\text{sp}^3$  bonded carbon C-C, C-O, and C=O chemical bonds in Fig. 8(d).<sup>54</sup> The deconvoluted high-resolution O 1s spectrum displays two peaks at 530.9 and 531.9 eV, corresponding to lattice oxygen in ZnO and surface-adsorbed species such as dissociated oxygen or hydroxyl groups,

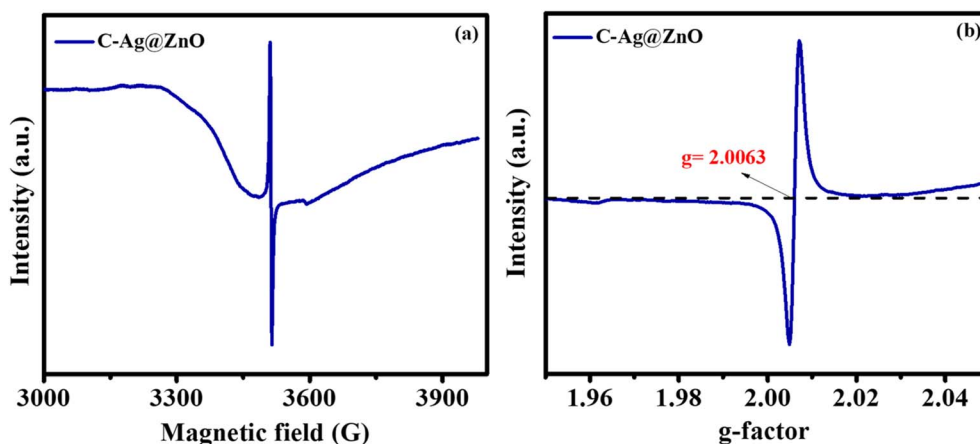


Fig. 9 EPR of C-Ag@ZnO (a) and (b)  $g$ -factor.



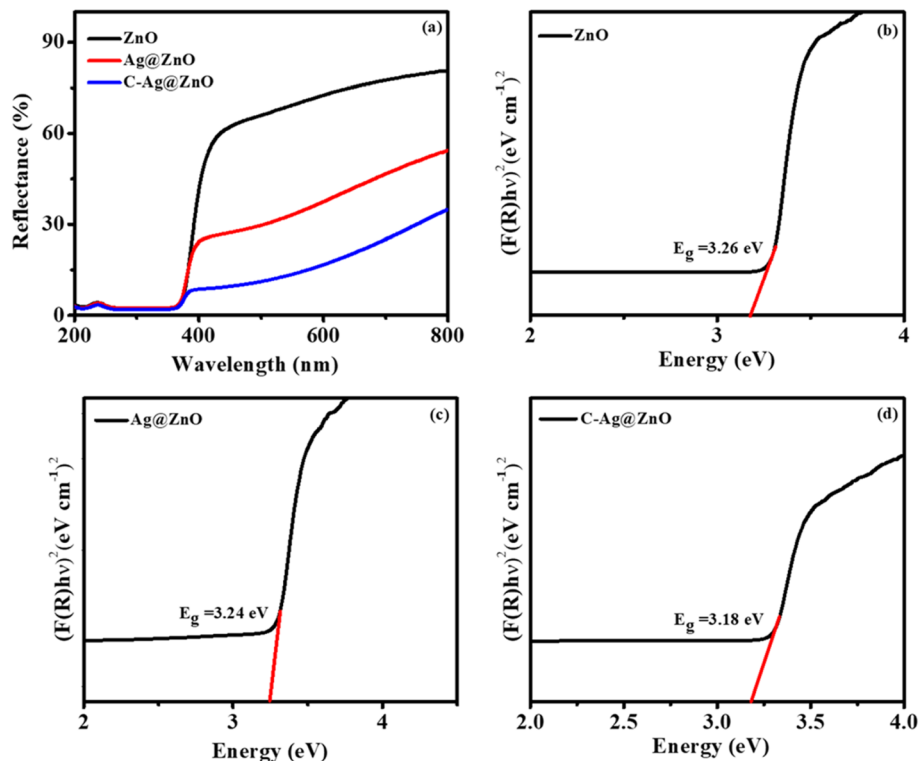


Fig. 10 UV-vis diffuse reflectance spectra of (a) ZnO, Ag@ZnO and C-Ag@ZnO. The plot of  $(F(R)h\nu)^2$  for ZnO (b), Ag@ZnO (c) and C-Ag@ZnO (d).

respectively. When photodegradation occurs, surface hydroxyl groups serve as dye adsorption sites, interacting with photo-generated holes to oxidize and form hydroxyl radicals, as shown in Fig. 8(e).<sup>53</sup>

### 3.4 Electron paramagnetic resonance (EPR) analysis

The samples were examined using *in situ* electron paramagnetic resonance (EPR) to confirm the presence and characteristics of C-Ag@ZnO composite oxygen vacancies (Fig. 9(a)). The presence of an oxygen vacancy is indicated by the strong signal of the C-Ag@ZnO composite, as shown in Fig. 9(b). According to earlier findings, the material with an oxygen vacancy should

have a matching *g* value of 2.0063. In order to improve the characteristics of C-Ag@ZnO materials and increase the separation efficiency of photo-excited charges, oxygen vacancies can be employed as electron capture centres.<sup>55,56</sup>

### 3.5 UV-DRS analysis

The UV-DRS spectra of the obtained materials in the diffuse reflectance mode (*R*) are shown in Fig. 10(a). In the visible light spectrum, the ZnO and Ag@ZnO materials had the maximum reflectance, but the C-Ag@ZnO compound showed lesser reflectance. An in-depth investigation of Fig. 10(b)–(d) indicates a decrease in the band gap energy values. The band gap values

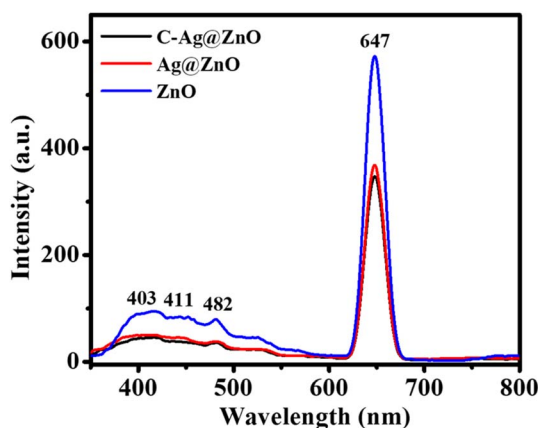


Fig. 11 PL emission spectra of ZnO, Ag@ZnO and C-Ag@ZnO.

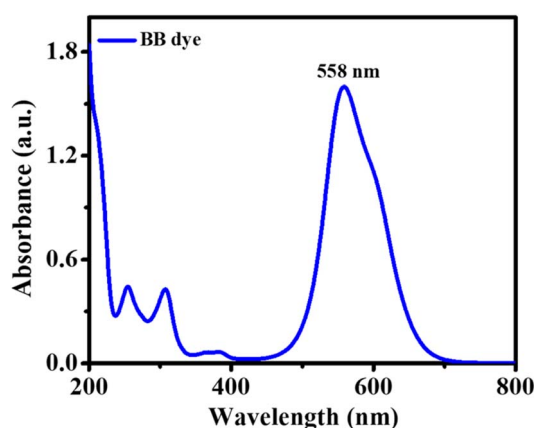


Fig. 12 UV absorption spectra of BB dye.





were calculated by the Kubelka–Munk function  $(F(R)E)^2$  against the energy of the adsorbed light ( $E$ ) using linear fits close to the absorption edge for obtaining the Tauc plots from the diffuse reflectance spectra.<sup>57–60</sup>

The slope of the Tauc plot is extended to the X-axis to get the semiconductor band gap. ZnO, Ag@ZnO, and C–Ag@ZnO nanocomposites have direct bandgaps ( $E_g$ ) of 3.26, 3.24, and 3.18 eV, respectively, according to calculations.

### 3.6 Photoluminescence (PL) study

The photoluminescence spectrum is a useful technique for analyzing the position of photogenerated electron ( $e^-$ ) and hole ( $h^+$ ) pairs, and the defects in metal semiconductor materials. The photoluminescence spectra of ZnO, Ag@ZnO and C–Ag@ZnO (Fig. 11) show weak emission peaks around 403, 411 and 482 nm and a strong peak around 647 nm. These peaks

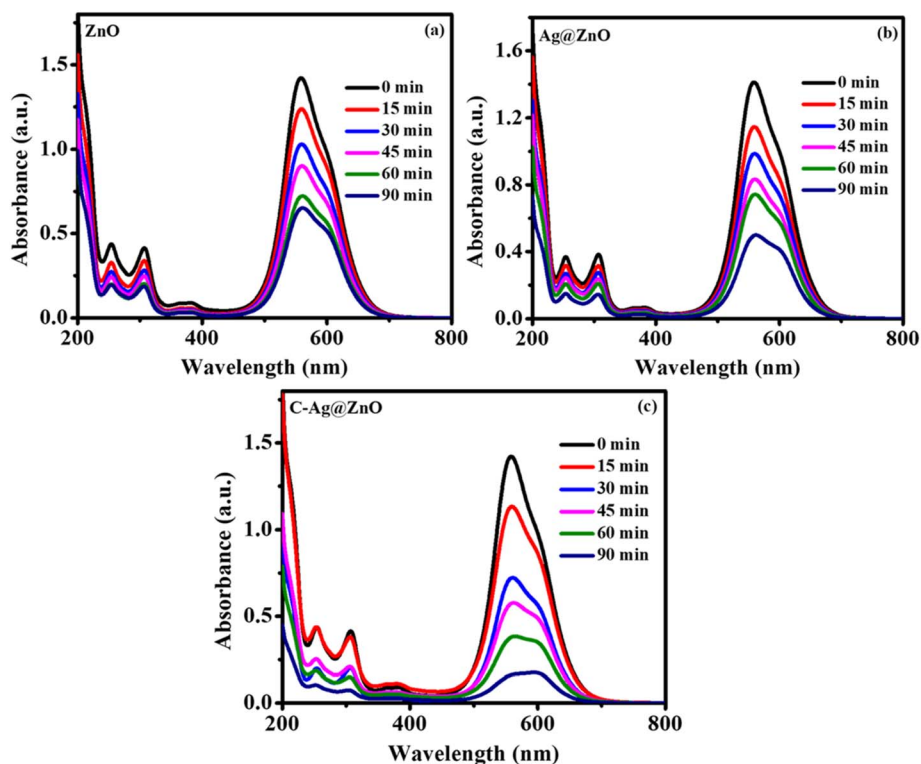


Fig. 13 Photodegradation of BB dye under UV-light by ZnO (a), Ag@ZnO (b) and C–Ag@ZnO (c).

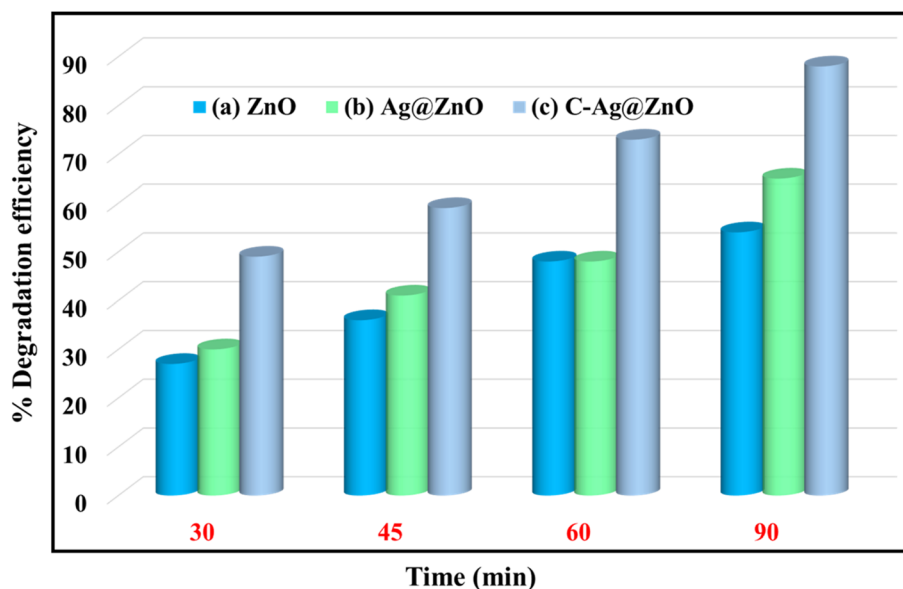


Fig. 14 Degradation efficiency percentage of ZnO (a), Ag@ZnO (b) and C–Ag@ZnO (c).



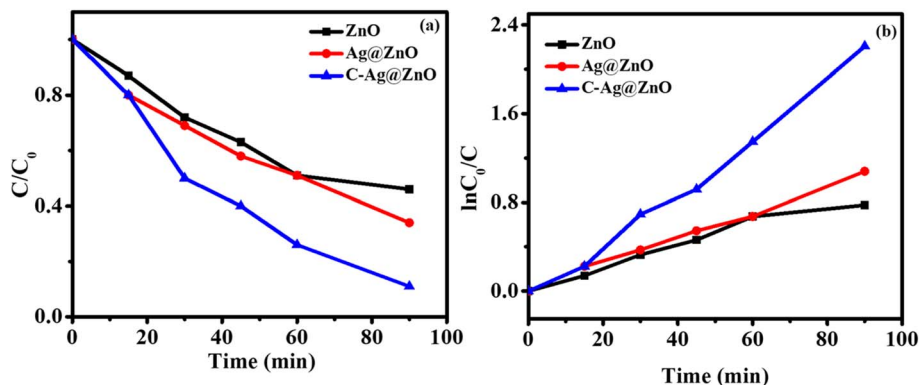


Fig. 15 (a, b) Kinetic graphs of ZnO, Ag@ZnO and C-Ag@ZnO catalysis.

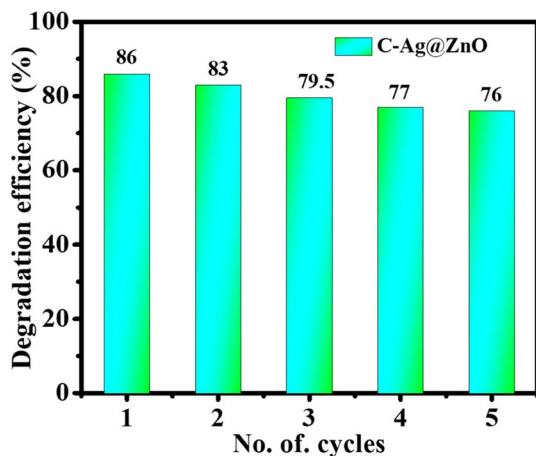


Fig. 16 C-Ag@ZnO degradation efficiency after one to five cycles.

reveal details about the levels of defects and charge carrier recombination. The near band edge emission (NBE) peaks in ZnO at about 403 and 411 nm are caused by bandgap excitation. The direct recombination of electrons in CB and holes in VB

produced blue emission at 482 nm and green emission at 647 nm. As the presence of Ag and carbon increases, the PL intensity decreases, indicating a longer lifetime and a slower rate of recombination of photoinduced charge carriers. Increased photocatalytic activity is revealed by the decrease in PL emission intensity, which is caused by improved electron transport, interfacial interaction between Ag, ZnO, and carbon, as well as a decreased rate of photoinduced charge recombination.<sup>61,62</sup>

### 3.7 Photocatalytic activity

When exposed to UV light, the photocatalytic efficiency of the prepared (ZnO, Ag@ZnO, and C-Ag@ZnO) catalysts was examined using BB dye. Fig. 12 shows that the Brilliant Blue (BB) dye in UV absorbance was measured, which shows strong absorbance at 558 nm. The UV absorbance was taken at different time intervals (0 to 90 min). After 90 min of radiation, ZnO degraded the dye to a 54.6% level. In Ag@ZnO, the degradation is only somewhat improved to 65.2%. Nevertheless, C-Ag@ZnO shows an increase of 88.6% deterioration within 90 min, as shown in Fig. 13. The photodegradation of the pollutant brilliant blue dye using the prepared catalyst as a photocatalyst under UV

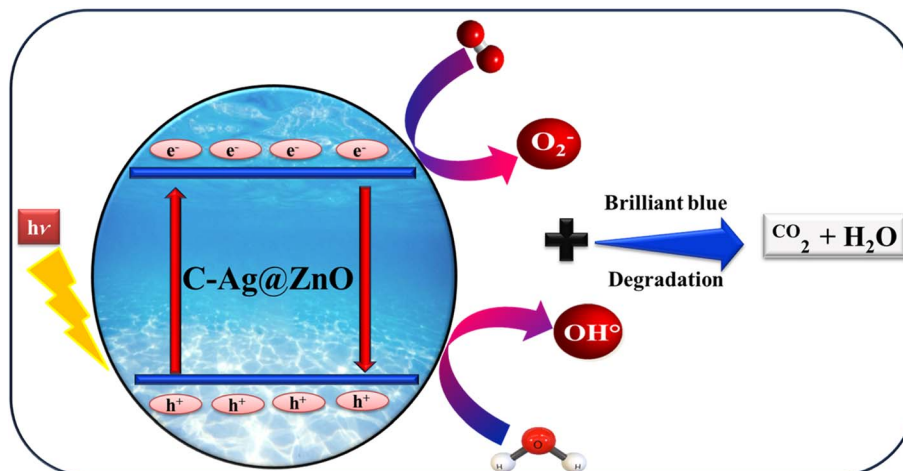
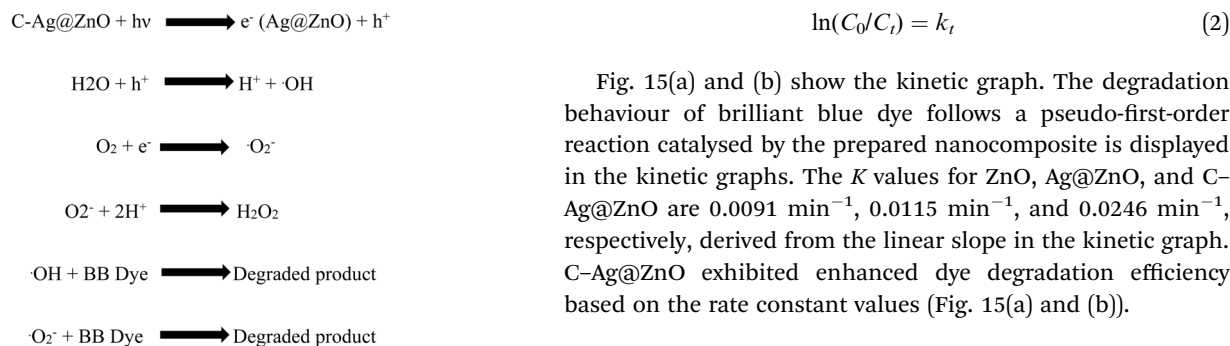


Fig. 17 Overall photodegradation mechanism.





Scheme 2 Dye degradation mechanism of the C-Ag@ZnO composite material.

chamber irradiation determined its ability to clean up contamination in the environment.

Typically, 100 mL of  $10^{-4}$  M BB dye solution with 0.100 g of catalyst was exposed to UV chamber radiation for 90 minutes. The prepared catalyst and Brilliant Blue dye were mixed in the dark for 15 minutes prior to exposure to UV light.

The data shown in Fig. 14 indicate that, when compared to ZnO and Ag@ZnO, C-Ag@ZnO exhibited the finest photocatalytic activity by degrading BB up to 88.6%.

### 3.8 Kinetic study

The following equation shows that the degradation of Brilliant Blue dye with a photocatalyst usually occurs in a pseudo-first-order reaction.

### 3.9 Reusability of the catalyst

Furthermore, as evidenced by the four subsequent runs of photocatalysis of the same C-Ag@ZnO composite, photocatalytic long-term durability in terms of reusability is very crucial for real-world applications. The photocatalytic degradation activity of the aqueous BB dye solution drops by around 3% during the second recycling run and by another 10% following the fifth recycling run, as shown in Fig. 16. The photocatalysis of the as-synthesised C-Ag@ZnO composite may be shown to have outstanding stability and reproducibility, which makes them appealing for photocatalytic nanomaterials with outstanding performance.

### 3.10 Mechanism of photocatalytic dye degradation

The absorption spectral changes of Brilliant Blue dye degradation catalysed by the C-Ag@ZnO photocatalyst (Fig. 17) could be explained as follows. The light source is hit on the valence band, and it accelerates the valence electrons ( $e^-$ ) into the conduction

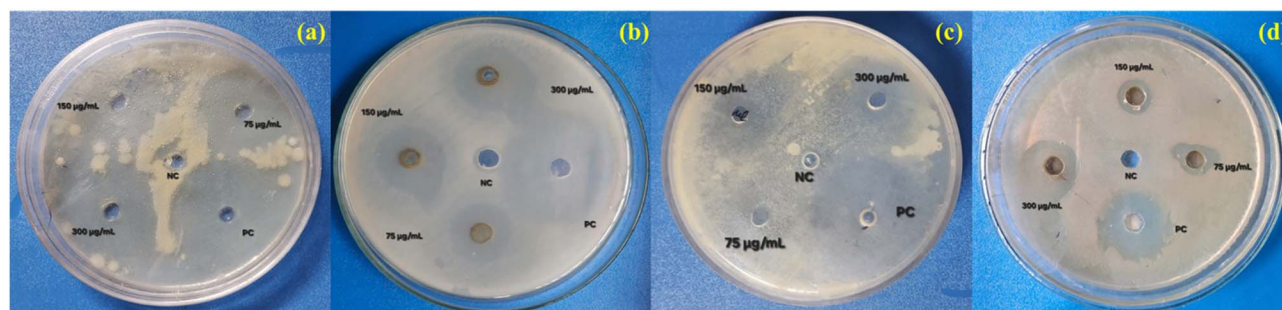


Fig. 18 Diagrammatic representations of the anti-bacterial activity of the synthesized C-Ag@ZnO nanocomposites.

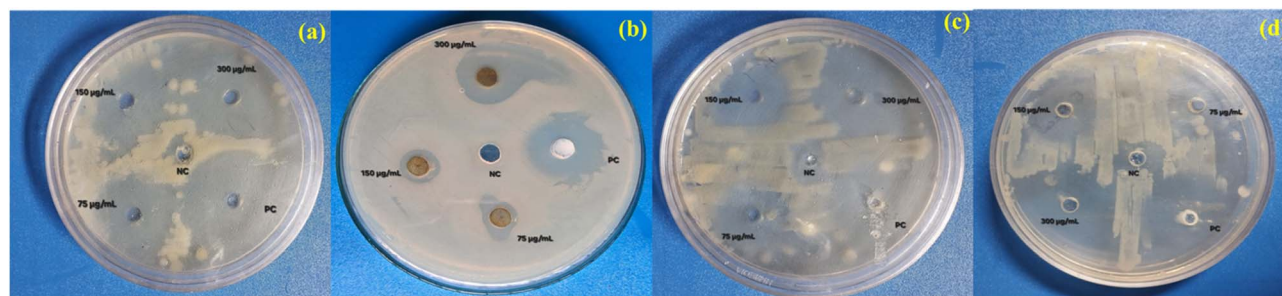


Fig. 19 Diagrammatic representations of the anti-bacterial activity of the synthesized Ag@ZnO nanocomposites.





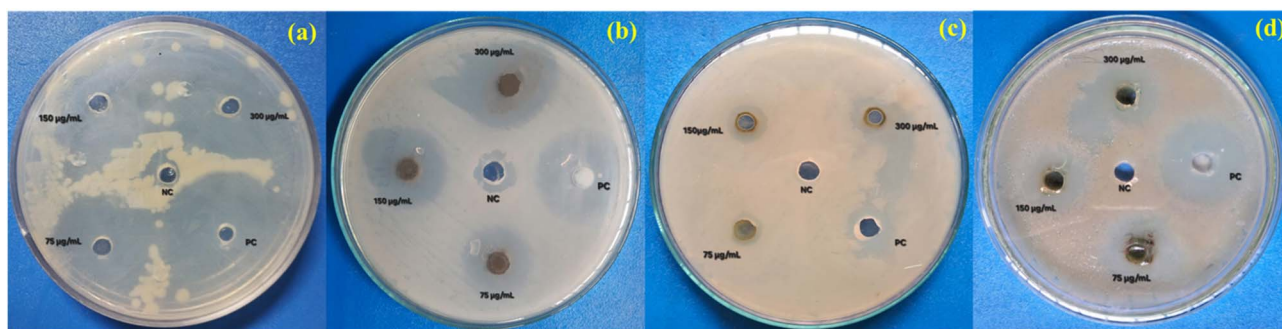


Fig. 20 Diagrammatic representations of the anti-bacterial activity of the synthesized Ag@ZnO nanocomposites.

band (CB), causing holes to develop in the valence band. In order to generate a solid oxidant, the photogenerated holes ( $h^+$ ) combine with  $H_2O$  to form the  $\cdot OH$  radical moiety. In the conduction band, the resulting electrons ( $e^-$ ) attach to the absorbed  $O_2$  to form superoxide anions ( $O_2^{\cdot -}$ ). This implies that  $H^+$  produces  $HO_2^{\cdot}$ , which is subsequently in charge of the

recombination electron's creation of the  $\cdot OH$  radical. The BB dye breaks down due to the energy-hungry free radicals (Scheme 2). The carbon material acts as a support and provides synergistic catalytic efficiency.<sup>63</sup>

### 3.11 Antibacterial activity

The antibacterial activity of ZnO, Ag@ZnO, and C-Ag@ZnO was measured using the Muller-Hinton agar plate method. Four pathogens were tested for this activity: Gram-positive strains of *Enterococcus faecalis* (*E. faecalis*) and *Bacillus subtilis* (*B. subtilis*) and Gram-negative strains of *Salmonella typhi* (*S. typhi*) and *Klebsiella pneumoniae* (*K. pneumoniae*). Using a micropipette, samples were added at three different concentrations (75  $\mu L$ , 150  $\mu L$ , and 300  $\mu L$ ) and incubated for 24 hours at  $30 \pm 2^\circ C$ . Ampicillin (5  $\mu L$ ) served as the positive control and DMSO as the negative control. A thorough analysis revealed that C-Ag@ZnO, which increases the bactericidal activity, is present in all three materials.<sup>64,65</sup> The effectiveness of the conventional antibiotic ampicillin is contrasted with the antibacterial visual evidence of the synthesized materials as shown in Fig. 18–20. Tables 1–3 display a comparable column chart and the observed results. As the result reveals, C-Ag@ZnO has good antibacterial activity when compared to other two compounds (ZnO and Ag@ZnO).

Table 1 Column chart of C-Ag@ZnO anti-bacterial activity results

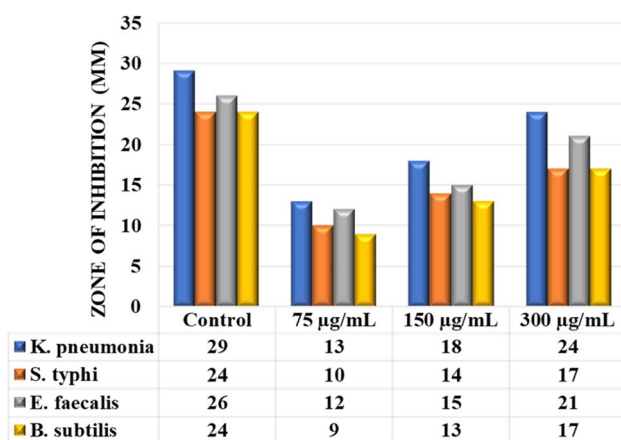


Table 2 Column chart of Ag@ZnO antibacterial activity results

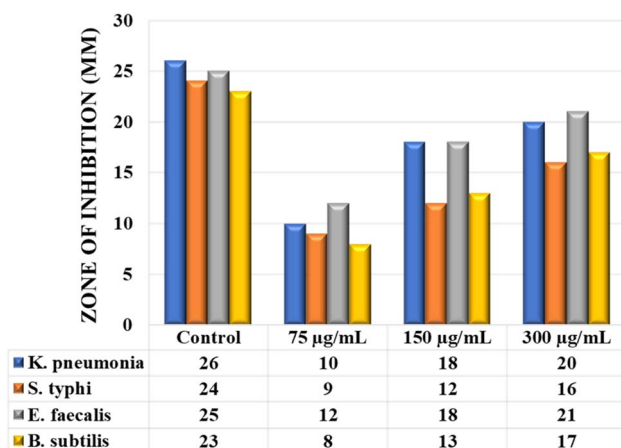
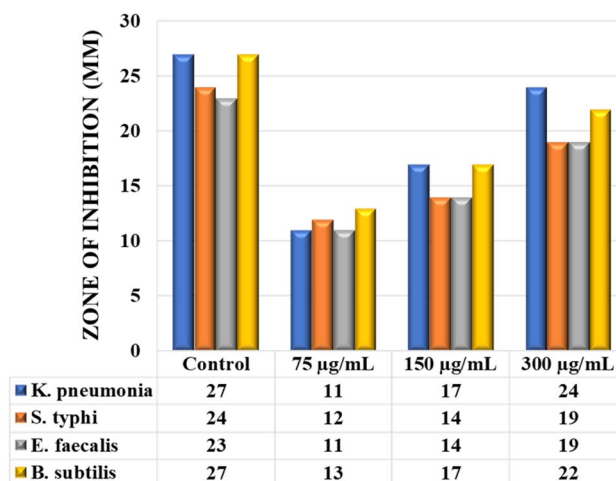


Table 3 Column chart of ZnO antibacterial activity results



## 4. Conclusion

In this study, novel self-assembled L-valine-derived carbon-assisted noble metal silver-doped zinc oxide nanoparticles were synthesized by a sol-gel method. This study effectively established C-Ag@ZnO as an outstanding photocatalytic and antibacterial active material. The as-prepared catalysts (ZnO, Ag@ZnO and C-Ag@ZnO) were characterized by various techniques, including XRD, FT-IR spectroscopy, RAMAN Spectroscopy, FESEM, HR-TEM, XPS, EPR, UV-DRS, PL and UV-vis spectroscopy, which confirmed the formation of carbon-assisted silver-doped zinc oxide. ZnO and Ag@ZnO were revealed to have less photocatalytic activity than C-Ag@ZnO with 88% efficiency towards BB dye degradation in the aqueous media. It also showed a low band gap energy of 3.18 eV. C and Ag on the ZnO surface facilitated the separation of charge carriers produced by photolysis and improved the degradation of contaminants by photocatalysis. Furthermore, C-Ag@ZnO showed a good antibacterial activity against Gram-positive strains of *Enterococcus faecalis* (*E. faecalis*) and *Bacillus subtilis* (*B. subtilis*) and Gram-negative strains of *Salmonella typhi* (*S. typhi*) and *Klebsiella pneumoniae* (*K. pneumoniae*), which makes it an ideal candidate for waste water clean-up carbonaceous supports from the self-assembled valine showing promising potential for making suitable carbon-supported photocatalysts.

## Data availability

All relevant data generated and analyzed during the current study are included in this article.

## Conflicts of interest

There are no conflicts to declare.

## References

- 1 J. Wang, C. Liu, S. Yang, X. Lin and W. Shi, *J. Phys. Chem. Solids*, 2020, **136**, 109164–109170.
- 2 L. Kaliraj, J. C. Ahn, E. J. Rupa, S. Abid, J. Lu and D. C. Yang, *J. Photochem. Photobiol.*, 2019, **199**, 111588–111594.
- 3 Z. Ali, S. Kiran, N. U. Haq, A. Dahshan, S. Z. Iqbal, A. Nazir, A. Munawar, A. L. Khan, N. Alwadai and M. Iqbal, *Mater. Chem. Phys.*, 2024, **315**, 128951–128958.
- 4 S. A. Ansari, N. Parveen, G. M. Alsulaim, A. A. Ansari, S. A. Alsharif, K. M. Alnahdi, H. A. Alali and V. R. M. Reddy, *Surf. Interface Anal.*, 2023, **40**, 103078–103088.
- 5 M. Aadil, A. Rahman, S. Zulfikar, I. A. Alsafari, M. Shahid, M. Shakir, P. O. Agboola, S. Haider and M. F. Warsi, *Adv. Powder Technol.*, 2021, **32**, 940–950.
- 6 S. A. Ansari, *Ceram. Int.*, 2023, **49**, 17746–17752.
- 7 K. Thakur, S. Kalia, B. S. Kaith, D. Pathania, A. Kumar, P. Thakur, C. E. Knittel, C. L. Schauer and G. Totaro, *J. Environ. Chem. Eng.*, 2016, **4**, 1743–1752.
- 8 M. Sharma, F. Monika, P. Thakur, R. V. Saini, R. Kumar and E. Torino, *Sci. Rep.*, 2020, **10**, 10934.
- 9 K. Sharma, A. Sudhaik, P. Raizada, P. Thakur, X. M. Pham, Q. Van Le, V. H. Nguyen, T. Ahamad, S. Thakur and P. Singh, *Environ. Sci. Pollut. Res. Int.*, 2023, **30**, 124902–124920.
- 10 C. W. Chang, H. T. Wu, S. H. Huang, C. K. Chen, I. W. Un and T. J. Yen, *Acta Mater.*, 2013, **61**, 6993–6999.
- 11 M. Francavilla, A. Pineda, A. A. Romero, J. C. Colmenares, C. Vargas, M. Monteleone and R. Luque, *Green Chem.*, 2014, **16**, 2876–2885.
- 12 M. S. Bakshi, P. Thakur, S. Sachar and T. S. Banipal, *Mater. Lett.*, 2007, **61**, 3762–3767.
- 13 A. Dhawan, A. Sudhaik, P. Raizada, S. Thakur, T. Ahamad, P. Thakur, P. Singh and C. M. Hussain, *J. Ind. Eng. Chem.*, 2023, **117**, 1–20.
- 14 T. Whang, M. Hsieh and H. Chen, *Appl. Surf. Sci.*, 2012, **258**, 2796–2801.
- 15 V. Srivastava, C. H. Weng, V. K. Singh and Y. C. Sharma, *J. Chem. Eng. Data*, 2011, **56**, 1414–1422.
- 16 A. Bodalo-Santoyo, J. L. Gómez-Carrasco, E. Gomez-Gomez, F. Maximo-Martin and A. M. Hidalgo-Montesinos, *Desalination*, 2003, **155**, 101–108.
- 17 N. Hanis, H. Hairrom, A. Wahab, A. Amir and H. Kadhum, *Chem. Eng. J.*, 2015, **260**, 907–915.
- 18 I. Rykowska, W. Wasiak and J. Byra, *Chem. Pap.*, 2008, **62**, 255–259.
- 19 M. A. Rauf and S. S. Ashraf, *Chem. Eng. J.*, 2009, **151**, 10–18.
- 20 R. Y. Hong, S. Z. Zhang, G. Q. Di, H. Z. Li, Y. Zheng, J. Ding and D. G. Wei, *Mater. Res. Bull.*, 2008, **43**, 2457–2468.
- 21 M. Fu, Y. Li, P. Lu, J. Liu and F. Dong, *Appl. Surf. Sci.*, 2011, **258**, 1587–1591.
- 22 M. Subburu, R. Gade, V. Guguloth, P. Chetti, K. R. Ravulapelly and S. Pola, *J. Photochem. Photobiol.*, A, 2021, **406**, 112996.
- 23 J. Ahemed, J. Pasha, R. Kore, R. Gade, Y. Bhongiri, P. Chetti and S. Pola, *J. Photochem. Photobiol.*, A, 2021, **419**, 113455.
- 24 K. Masula, Y. Bhongiri, G. R. Rao, P. V. Kumar, S. Pola and M. Basude, *Opt. Mater.*, 2022, **126**, 112201.
- 25 T. Whang, M. Hsieh and H. Chen, *Appl. Surf. Sci.*, 2012, **258**, 2796–2801.
- 26 H. Y. Wu, W. J. Jian, H. F. Dang, X. F. Zhao, L. Z. Zhang and J. H. Li, *Pol. J. Environ. Stud.*, 2017, **26**, 871–880.
- 27 Z. Lu, W. Xu, W. Zhu, Q. Yang, X. Lei, J. Liu, Y. Li, X. Sun and X. Duan, *Chem. Commun.*, 2014, **50**, 6479–6482.
- 28 K. Ravichandran, R. Mohan, B. Sakthivel and S. Varadharajaperumal, *Appl. Surf. Sci.*, 2014, **321**, 310–317.
- 29 G. Borkow, R. C. Zatcoff and J. Gabbay, *Med. Hypotheses*, 2009, **73**, 883–886.
- 30 T. Tang, C. Li, W. He, W. Hong, H. Zhu, G. Liu, Y. Yu and C. Lei, *J. Alloys Compd.*, 2022, **894**, 162559–162570.
- 31 W. Yu, J. Zhang and T. Peng, New insight into the enhanced photocatalytic activity of N-, C- and S-doped ZnO photocatalysts, *Appl. Catal., B*, 2016, **181**, 220–227.
- 32 H. Wang, C. Xie, W. Zhang, S. Cai, Z. Yang and Y. Gui, *J. Hazard. Mater.*, 2007, **141**, 645–652.
- 33 R. Y. Hong, S. Z. Zhang, G. Q. Di, H. Z. Li, Y. Zheng, J. Ding and D. G. Wei, *Mater. Res. Bull.*, 2008, **43**, 2457–2468.



- 34 M. Fu, Y. Li, P. Lu, J. Liu and F. Dong, *Appl. Surf. Sci.*, 2011, **258**, 1587–1591.
- 35 R. S. Sabry, M. I. Rahmah and W. J. Aziz, *J. Mater. Sci.: Mater. Electron.*, 2020, **31**, 13382–13391.
- 36 D. Kwon and J. Kim, *Korean J. Chem. Eng.*, 2020, **37**, 1226–1232.
- 37 R. Ebrahimi, K. Hossienzadeh, A. Maleki, R. Ghanbari, R. Rezaee, M. Safari, B. Shahmoradi, H. Daraei, A. Jafari, K. Yetilmezsoy and S. H. Puttaiah, *J. Environ. Health. Sci. Eng.*, 2019, **17**, 479–492.
- 38 A. Gnanaprakasam, V. M. Sivakumar and M. Thirumarimurugan, *Water Sci. Technol.*, 2016, **74**, 1426–1435.
- 39 K. Pradeev Raj, K. Sadaiyandi, A. Kennedy, S. Sagadevan, Z. Z. Chowdhury, M. R. B. Johan, F. A. Aziz, R. F. Rafique, R. Thamiz Selvi and R. Rathina Bala, *Nanoscale Res. Lett.*, 2018, **13**, 1–13.
- 40 R. Naveenkumar, B. Karthikeyan and S. Senthilvelan, *Braz. J. Phys.*, 2024, **54**, 170–191.
- 41 M. Anwar, Z. N. Kayani and A. Hassan, *Opt. Mater.*, 2021, **118**, 111276–111289.
- 42 I. H. Ifijen, M. Maliki and B. Anegebe, *OpenNano*, 2022, **8**, 100082–100106.
- 43 A. Phuruangrat, T. Thongtem and S. Thongtem, Microwave-assisted synthesis of ZnO nanostructure flowers, *Mater. Lett.*, 2009, **63**, 1224–1226.
- 44 U. T. Khatoon, K. V. Rao, J. R. Rao and Y. Aparna, *Iconset*, 2011, 97–99.
- 45 K. P. Sapkota, I. Lee, M. A. Hanif, M. A. Islam and J. R. Hahn, *Catalysts*, 2019, **9**, 498–511.
- 46 D. A. Bopape, D. E. Motaung and N. C. Hintsho-Mbita, *Textiles*, 2024, **4**, 104–125.
- 47 H. A. H. Alshamsi and B. S. Hussein, *Orient. J. Chem.*, 2018, **34**, 1898–1907.
- 48 S. R. Verma, A. Chauhan, M. Shandilya, X. Li, R. Kumar and S. Kulshrestha, *J. Environ. Chem. Eng.*, 2020, **45**, 103730–103736.
- 49 H. M. Cheng, K. F. Lin, C. J. Hsu Lin, L. J. Lin and W. F. Hsieh, *J. Phys. Chem. B*, 2005, **109**, 18385–18390.
- 50 A. Ullah, M. Saadullah, F. Alvi, L. Sherin, A. Ali, N. A. Shad, Y. Javed, M. M. Sajid, G. Yasin and W. Abbas, *J. King Saud Univ. Sci.*, 2022, **34**, 101724–101730.
- 51 D. A. Bopape, D. E. Motaung and N. C. Hintsho-Mbita, *Textiles*, 2024, **4**, 104–125.
- 52 S. Demirci, T. Dikici, M. Yurddaskal, S. Gultekin, M. Toparli and E. Celik, *Appl. Surf. Sci.*, 2016, **390**, 591–601.
- 53 B. Xin, L. Jing, Z. Ren, B. Wang and H. Fu, *J. Phys. Chem., B*, 2005, **109**, 2805–2809.
- 54 A. Dolgov, D. Lopaev, C. J. Lee, E. Zoethout, V. Medvedev, O. Yakushev and F. Bijkerk, *Appl. Surf. Sci.*, 2015, **353**, 708–713.
- 55 J. Zhang and J. Li, *Nanomaterials*, 2022, **12**, 433.
- 56 E. Erdem, *J. Alloys Compd.*, 2014, **605**, 34–44.
- 57 P. Kubelka and F. Munk, *Z. Tech. Phys.*, 1931, **12**, 593–601.
- 58 P. Kubelka, *J. Opt. Soc. Am.*, 1948, **38**, 448–457.
- 59 M. P. Fuller and P. R. Griffiths, *Anal. Chem.*, 1978, **50**, 1906–1910.
- 60 S. Ratchawong, S. Wacharawichanant and S. Tanodekaew, *Mater. Sci. Forum*, 2020, **998**, 96–101.
- 61 M. Ahmad, I. Ahmad, E. Ahmed, M. S. Akhtar and N. R. Khalid, *J. Mol. Liq.*, 2020, **311**, 113326–113337.
- 62 A. A. Sharwani, K. B. Narayanan, M. E. Khan and S. S. Han, *Sci. Rep.*, 2022, **12**, 10017–10034.
- 63 M. Subburu, R. Gade, M. Basude, P. Chetti, N. B. Simhachalam, P. Nagababu, Y. Bhongiri and S. Pola, *Environ. Sci.: Water Res. Technol.*, 2021, **7**, 1737–1747.
- 64 R. Gade, J. Ahemed, K. L. Yanapu, S. Y. Abate, Y. T. Tao and S. Pola, *J. Environ. Chem. Eng.*, 2018, **6**, 4504–4513.
- 65 R. Gade, M. Basude, N. B. Simhachalam, S. Pola and P. Chetti, *Environ. Sci.: Water Res. Technol.*, 2022, **8**, 3065–3078.

